基于分束棱镜分光的共路离轴数字全息显微术研究

王华英[1,2*]，雷家良[1]，王学[1,2]，王文健[1]，张子健[1]，王杰宇[1]，董昭[1,2]

[1]河北工程大学数理科学与工程学院，河北 邯郸 056038；
[2]河北省计算光学成像与光电检测技术创新中心，河北 邯郸 056038

摘要 提出了一种基于分束棱镜分光的共路离轴数字全息光路系统，该系统不仅能任意调节物光光强与参考光光强的比值，还可以灵活调节全息图频谱三项分离的距离，解决了传统针孔滤波共路离轴数字全息系统记录的全息图条纹对比度不高和记录器件的空间带宽积利用率不充分的问题。在理论和实验上分析了系统调试条纹对比度和频谱三项距离的可行性，介绍了相应的调节方法，并通过实验分析验证了该系统的成像性能。

关键词 全息；数字全息技术；显微术；定量相位测量；频谱滤波

中图分类号 O436　　**文献标志码** A　　　　　　　　　　**DOI**：10.3788/CJL202249.1309002

1 引　　言

数字全息显微技术是一种结合了显微术、全息术以及计算机科学的高质量成像技术，该技术能在无接触、无染色的实验条件下对相位物体及各类微结构进行实时定量成像与可视化测量[1-3]，不仅可以保证被测物体的完整性和无侵害，而且能够方便地进行数字滤波、自动聚焦、畸变校正、存储与传输等处理[4-7]。因此，数字全息显微已经成为一种非常重要的三维定量显微成像与可视化检测工具[8-9]，在生命[10-11]、医药[12-13]、环境[14]、材料[15-16]、制造[17]等领域发挥着重要作用。

常用的数字全息显微成像系统是基于马赫-曾德尔光路结构的离轴数字全息系统[18]，该系统抗外界干扰能力弱，稳定性差，且使用的光学元件较多。共路离轴数字全息显微术中物光与参考光经过了相同的光学元件，外界扰动使两束光引入相同的相位噪声，因此，该光路具有很强的稳定性，近年来在国际上获得了广泛关注[19-31]。共路离轴数字全息光路系统主要分两种：一种是基于分光元件和空间滤波器相结合的结构[19-24]，另一种是基于分光元件而无需滤波器的结构[25-31]。常用的是第一种光路结构，这种结构由麻省理工学院的 Popescu 等[19-20]于 2006 年首次提出，其中包含物体信息的光束被分光元件分成两束或多束，空间滤波器将其中的一束光滤波成只包含直流信息的参考光波，该参考光波与另外一束包含物体信息的物光波被透镜准直后在光电传感器光敏面上发生干涉。系统的一维余弦型振幅光栅作为分光元件将光束分为三束，光栅的 0 级衍射光经针孔滤波后形成参考光，+1 或−1 级衍射光作为物光束，这两束光经透镜准直合束后发生干涉形成全息图。第二种共路离轴数字全息显微系统由 Mico 等[31]于 2014 年提出，该系统能使照明光波同时照射有样品的区域和无样品的区域，然后通过分光元件将光束分成两束或多束，并使得其中一束光中包含物体信息的区域与另一束光中无样品区域相重叠发生干涉形成全息图。其中分光元件也是一维余弦型振幅光栅。这种光路结构最大的缺点是成像视场仅占显微物镜视场的四分之一，这有悖于显微成像高分辨率、大视场的需求。目前，分光元件分光和空间滤波器滤波相结合的共路离轴数字全息显微术仍然是国际重要的前沿研究领域。

传统的共路离轴数字全息显微术虽然能够用于活体样品长期稳定的观测，但还存在以下缺点：参考光光强比物光光强弱，无法充分满足全息图记录条件，干涉条纹对比度差；当光栅参数确定后，物光束与参考光束之间的夹角即被确定了下来，因此，不能根据实验所需灵活调节两束光分离的距离；此外，该系统元件确定后，不能根据样品的需求灵活调节干涉条纹对比度。Zhang 等[32]在 2020 年搭建了一种基于偏振光栅的共路离轴数字全息显微系统[32]，系统通过四分之一波片和偏振光栅的偏振特性，实现了物光与参考光分光比的灵活调节，然而该系统受限于光栅的分光能力，+1级频谱滤波操作受影响，难以充分利用记录器件的空

间带宽积。2020 年 Kumar 等[24]搭建了一种采用分光棱镜的共路离轴全息系统,并分析了该新型分光系统的成像能力,但是该光路结构无法解决物光与参考光光强比低的缺陷,并且文章并未具体分析该系统在分光能力上的优势。本文上述两种光路结构,搭建了一种共路离轴数字全息显微系统,该系统能解决传统共路离轴数字全息显微系统存在的上述问题。我们相信该研究有助于共路离轴数字全息显微镜的研究与发展。

2　实验原理与方法

实验光路如图 1(a)所示,该光路由照明系统、显微放大系统、分束滤波系统以及干涉记录系统四部分构成。半导体激光器(波长 $\lambda = 532$ nm)、半波片(DW)、空间滤波器及透镜 L_1(焦距 $f_1 = 60$ mm)组成照明系统,该系统将激光器发射的光束扩束准直,并使光束垂直照射到样品平面。物镜(MO,放大倍率为40,数值孔径 NA 为 0.60)和透镜 L_2(焦距 $f_2 = 100$ mm)构成显微放大系统,该系统将光束中携带的物体信息进行放大并使光束沿主轴方向传播。透镜 L_3(焦距 $f_3 = 150$ mm)、分束棱镜(BS)以及针孔滤波器(直径 $d = 50$ μm)构成分束滤波系统,系统中的分束棱镜将入射的光束分成两束,其中透射经过 BS 的光作为参考光,反射经过 BS 的光束作为物光。具体来说,物光波仍保留物体信息,但参考光波被针孔滤波器滤波后只保留了其中的直流信息。L_4(焦距 $f_4 = 100$ mm)、偏振片和互补金属氧化物半导体图像传感器(CMOS,像素数为 1280×1024)组成干涉记录系统,分离的物光与参考光经过该系统时被其中的 L_4 会聚,会聚的光束经过偏振片后在 CMOS 光敏面上发生干涉形成全息图。图 1(a)中的透镜 L_3 和 L_4 构成了 $4f$ 系统,针孔位于系统的空间频谱面上,对光束进行滤波,其中 M 为反射镜,P 为偏振片。最后 CMOS 将全息图传输至计算机进行处理。图 1(b)展示的是模拟的三维图。
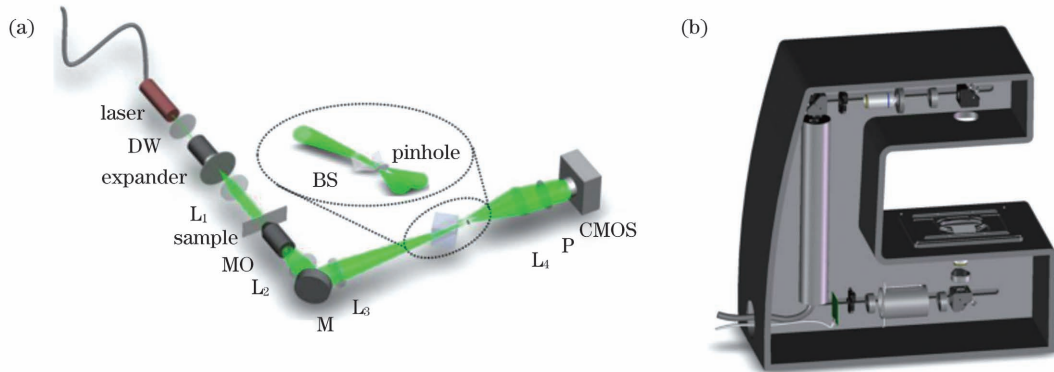

图 1　实验光路示意图及显微镜三维展示图。(a)光路示意图;(b)显微镜三维展示图

Fig. 1　Schematic of experimental optical path and 3D map of microscope. (a) Schematic of optical path; (b) 3D map of microscope

2.1　频谱分离距离的调控

假设被分束棱镜分离的两束光到达 L_3 后焦面时,光斑中心相距 l,考虑到物光束沿着系统的主轴传播,则参考光被分束棱镜调制的空间频率[20]可以表示为

$$\beta = 2\pi l / \lambda f_3 。 \tag{1}$$

受记录器件 CMOS 像元尺寸以及频谱分离的限制,干涉条纹必须满足 Nyquist 采样定理,且频谱必须满足三项分离原则[33]。因此,被分束棱镜调制后,在频谱面上得到的参考光载频取值区间为

$$3k_0 NA_{obj}/M_{obj} \leqslant \beta \leqslant \pi M_{4f}/a - k_0 NA_{obj}/M_{obj}, \tag{2}$$

式中:$k_0 = 2\pi/\lambda$;NA_{obj} 表示物镜的数值孔径;M_{obj} 表示物镜的放大倍率;M_{4f} 表示 $4f$ 系统的放大倍率;α 表示图像传感器的像元尺寸。由式(1)、(2)联立得到 l 的取值范围为

$$3NA_{obj}f_3/M_{obj} \leqslant l \leqslant (\lambda M_{4f}/a - NA_{obj}/M_{obj})f_3 。 \tag{3}$$

假设入射光与分束棱镜入射面的法线夹角为45°,且 BS 分束膜正好与光轴处于同一平面,光束传输示意图如图 2 所示,其中 θ_1、θ_2 分别为入射角和入射时的折射角,θ_2'、θ_1' 分别为出射角和出射时的折射角,且 $\theta_2 = \theta_2'$,$\theta_1 = \theta_1'$。
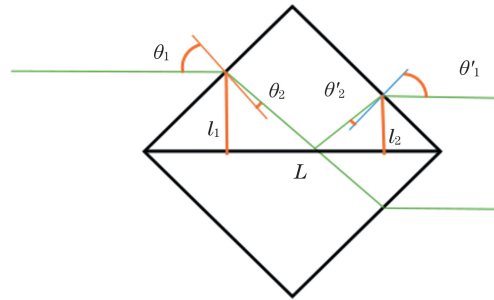

图 2　光束通过分光棱镜传输的示意图

Fig. 2　Schematic of beam transmission through splitter

在图 2 中,入射光相对分光膜的横向偏移距离 l_1 与出射光相对分光膜的横向偏移距离 l_2 的关系为

$$L = l_1 + l_1 \tan[\arcsin(\sin\theta_1/n) + \pi/4] + l_2 + l_2 \tan[\arcsin(\sin\theta_1'/n) + \pi/4], \tag{4}$$

式中:n 为分束棱镜折射率;L 为 BS 分束膜的长度。根据上述理论分析,实验可通过横向移动分束棱镜,调

节入射光束相对于分光膜的横向偏移距离 l_1，分离的物参光的相对距离 $2l_2$ 也会改变，最终影响频谱三项分离距离。

由式（3）计算可知，两光束的中心距离 $2l_2$ 在 $6.75\sim9.19$ mm 范围内时，该区间会发生频谱混叠，超过该区间采样条件不满足，发生频谱折叠。实验中用的分束棱镜折射率 $n=1.519$，$L=35.5$ mm，实验时保证 $\theta_1=\theta_1'=45°$，通过式（4）计算，可知横向调节的入射光相对分光膜的横向偏移 l_1 需要在 $7.22\sim8.43$ mm 范围内。

2.2 可控条纹的对比度

假设半导体激光器发出偏振态为 $\begin{bmatrix}\cos\theta\\\sin\theta\end{bmatrix}$ 的线偏振光（其中 θ 表示偏振光振动方向与水平方向的夹角），光束经过半波片时偏振特性从初始态变成关于半波片主轴方向对称的偏振状态[34]，根据该特性，旋转半波片可灵活调节激光偏振方向，理想情况是该激光通过半波片后被调试成偏振状态为 $\begin{bmatrix}1\\1\end{bmatrix}$ 的光束，如图 3（a）所示。经过分束棱镜的透射光以及反射光的偏振态关于分光膜所处平面对称，利用琼斯矩阵可分别表示为 $\begin{bmatrix}1\\1\end{bmatrix}$、$\begin{bmatrix}1\\-1\end{bmatrix}$，如图 3（b）所示。物参光经过偏振片后，偏振方向与偏振片的主轴方向相同，如图 3（c）所示。发生干涉时物光与参考光偏振态的琼斯矩阵表示为

$$
\begin{aligned}
\widetilde{\boldsymbol{O}} &= \begin{bmatrix} \cos^2\theta' & \sin\theta'\cos\theta' \\ \cos\theta'\sin\theta' & \sin^2\theta' \end{bmatrix} \begin{bmatrix} 1 \\ 1 \end{bmatrix} = \begin{bmatrix} \cos^2\theta' + \sin\theta'\cos\theta' \\ \sin^2\theta' - \sin\theta'\cos\theta' \end{bmatrix} \\
\widetilde{\boldsymbol{R}} &= \begin{bmatrix} \cos^2\theta' & \sin\theta'\cos\theta' \\ \cos\theta'\sin\theta' & \sin^2\theta' \end{bmatrix} \begin{bmatrix} 1 \\ -1 \end{bmatrix} = \begin{bmatrix} \cos^2\theta' - \sin\theta'\cos\theta' \\ \cos\theta'\sin\theta' - \sin^2\theta' \end{bmatrix}
\end{aligned}
\tag{5}
$$

式中：θ' 表示偏振片主轴方向与水平方向之间的夹角。根据式（5）与马吕斯定律可知，物光与参考光偏振态随 θ' 的变化而发生改变，从而影响物光与参考光的光强。图 3（a）、（b）、（c）展示的分别是半波片、分束棱镜、偏振片对光束偏振态的调节示意图，图 3（d）、（e）分别是在不同 θ' 下物光与参考光光强的变化以及干涉条纹对比度的变化情况。

物光与参考光的强度比会直接影响干涉条纹的对比度，通过调节 θ'，可最大程度改善干涉条纹的清晰度。物光与参考光光强随 θ' 的变化如图3（d）所示，两

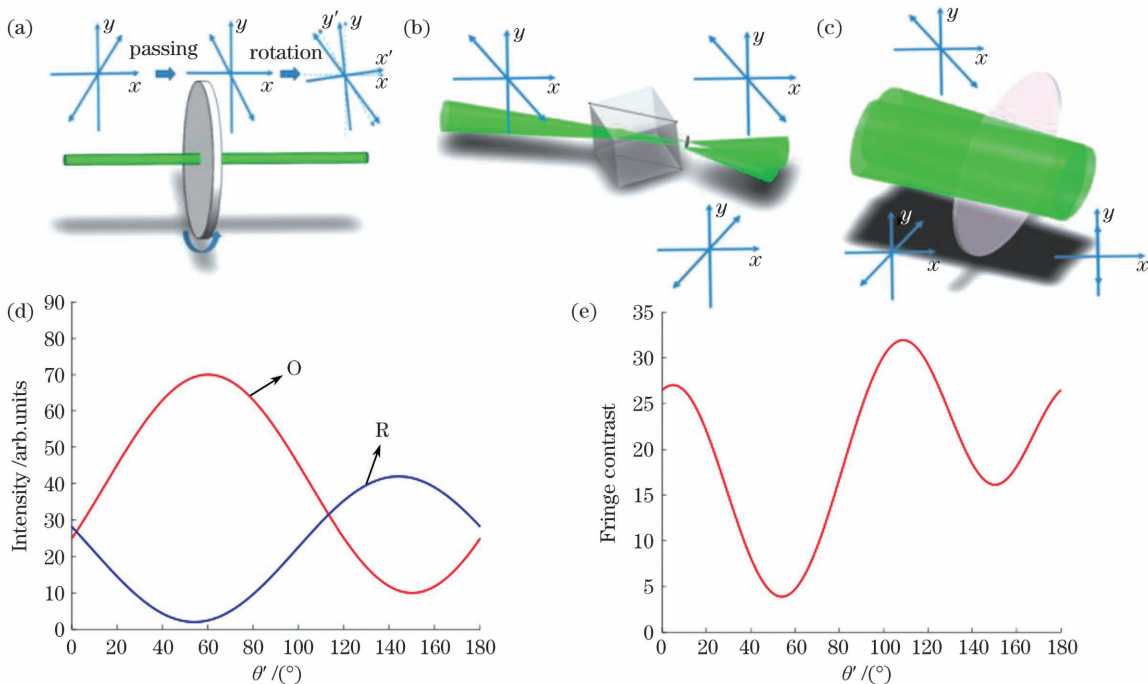图 3 BS 与偏振元件对光束偏振态和系统干涉条纹对比度的影响。（a）DW 调节入射的光束和偏振态变化图；（b）BS 将入射光束分离成两束及光束的偏振态变化图；（c）偏振片调节入射的两束光及偏振态变化图；（d）物光光强和参考光光强随 θ' 的变化；（e）条纹对比度随 θ' 的变化

Fig. 3 Influence of BS and polarization elements on polarization state of beam and interference fringe contrast of system. (a) Schematic of adjusting incident beam via DW and polarization state change; (b) schematic of splitting of incident beam into two beams via BS and polarization state change of beams; (c) schematic of adjusting incident two beams via polarizer and polarization state change; (d) object light intensity and reference light intensity versus θ'; (e) fringe contrast versus θ'

束光干涉后的条纹对比度随 θ' 的变化如图 3(e)所示。

3 实验结果与分析

3.1 系统调控性能的测试

实验样品选用直径标称值为 $(9.8\pm0.2)\mu m$ 的高度分散聚苯乙烯微珠(折射率为 1.593),将微珠样品浸没在位于载玻片上的折射率匹配油中,并采用本文的光路系统进行了实验研究。利用角谱重建算法获取强度图和相位图,采用基于横向剪切的最小二乘解包裹算法[35-36]对相位进行解包裹处理。图 4 为不同物参光分离距离下的实验结果。图 4(a)和图 4(f)分别是

针孔平面光束的分离距离为 5.0 mm 和 9.0 mm 时获取的全息图,图 4(b)、(d)是图 4(a)的频谱图(但滤波区域大小不同,见图中红色矩形框),图 4(g)是图 4(f)的频谱图,图 4(c)、(e)是由图 4(b)、4(d)重建得到的相位图,图 4(h)是由图 4(g)重建得到的相位图。由频谱图 4(b)、(d)和图 4(g)对比可知:光路中若物光与参考光的分离不充分,频谱会出现混叠;若频谱滤波区域过大,包括零级中心,零级信息会对重建图像产生严重的干扰,导致相位图中引入条纹信息。即使滤波区域减小,仍会引入零级谱的低频信息,给重建的相位图像带来噪声干扰。
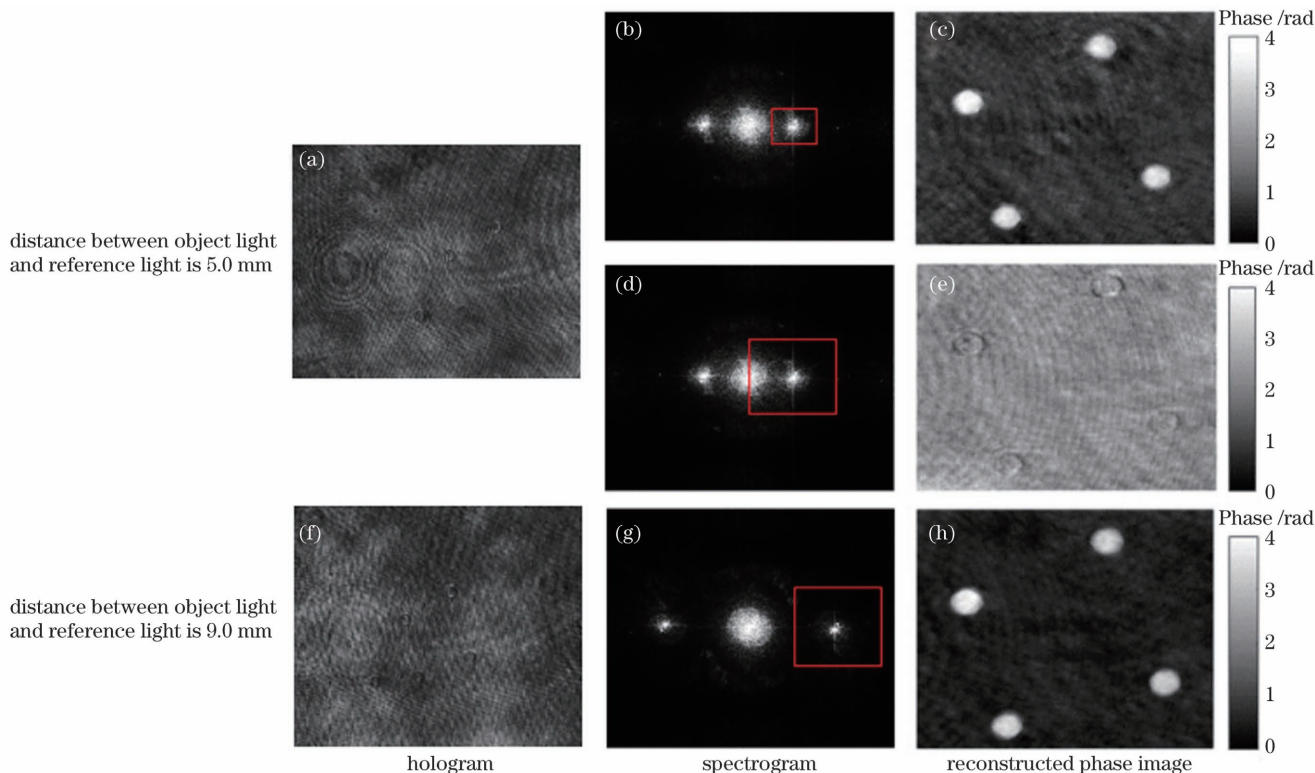

图 4 不同分光距离下的微珠实验结果

Fig. 4 Experimental results of polystyrene microsphere at different optical separation distances

为了模拟棱镜轴向旋转时频谱沿对角分布的情况,将 CMOS 轴向旋转了 45°。为保持实验变量的单一性,实验在照明光强不变的条件下,通过调节偏振片来改变参考光与物光的相对光强比,得到图 5 所示的实验结果。当物光与参考光的光强比被分别调制为 1∶1、6∶1 和 34∶1 时,获得的全息图以及相同区域的局部放大图如图 5(a)、(e)、(i)所示。对比可以看出,随着光强比的增大,全息图的条纹清晰度明显降低,符合图 3(e)的条纹清晰度变化趋势。从图 5(b)、(f)、(j)可以看出,随着物光与参考光光强比的增大,±1 级频谱展宽减小。由图 5(c)、(g)、(k)、(d)、(h)、(l)可以看出,物光与参考光光强比越大,物光携带的噪声会越来越明显,对重建图的质量影响也越来越大。

对比图 4、5 中频谱图可知,受记录器件光敏面形状的影响,在不发生频谱混叠的情况下,对角方向具有更多的频谱滤波利用空间,能避免频谱沿水平或者纵

向分布时可能引起的折叠情况。上述实验证明了两种光路调节方法的正确性和必要性。

3.2 系统成像性能的测试

微珠作为优秀的定量测试样品,是衡量系统成像准确性的首选实验对象。实验选用直径标称值为 $(9.8\pm0.2)\mu m$ 的高度分散聚苯乙烯微珠(折射率为 1.593)。采用上述光路以及微珠样本,得到的全息图如图 6(a)所示,图 6(b)、(c)、(d)分别是全息图所选范围的局部放大图、频谱图及重建获得的相位图。微珠厚度为

$$h = \frac{\Delta\varphi \times \lambda}{2\pi\Delta n}, \qquad (6)$$

式中:h 是微珠的厚度;$\Delta\varphi$ 是相位差;Δn 是微珠与折射率匹配溶液的折射率差。图 6(e)显示的是图 6(c)中白线部分的厚度曲线图,其中横轴零点为图 6(c)中白线左端点。由微珠厚度曲线的最高点值可知,重建
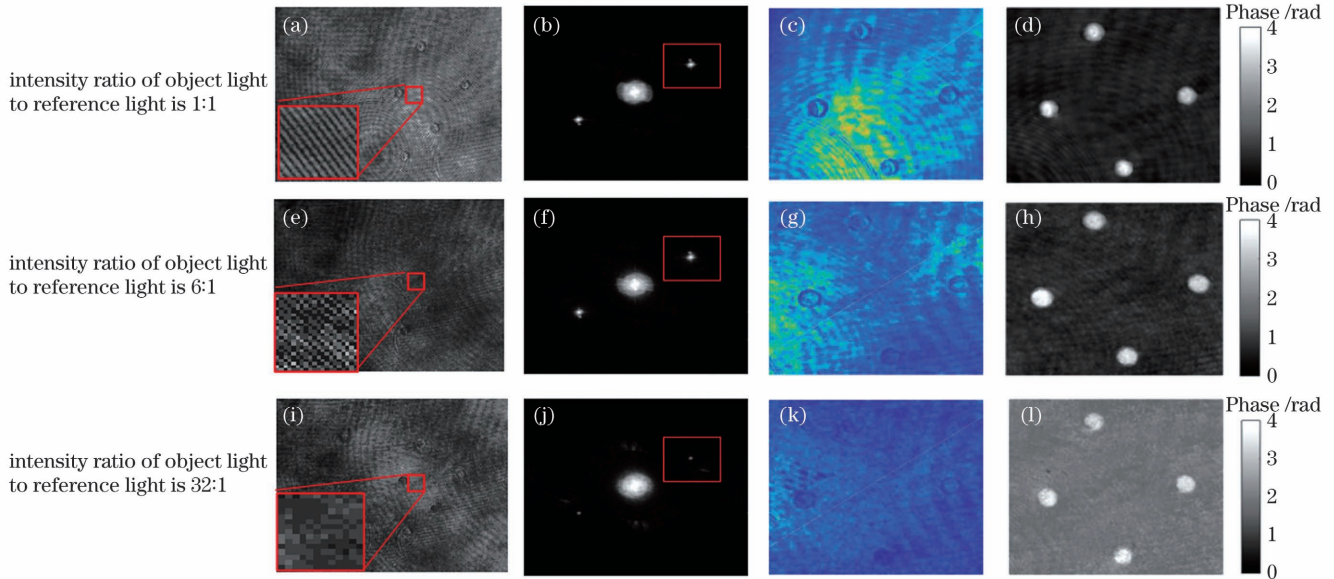
图 5　不同参考光与物光光强比下得到的微珠实验图

Fig. 5　Experimental results of polystyrene microsphere obtained under different light intensity ratios of reference light and object light
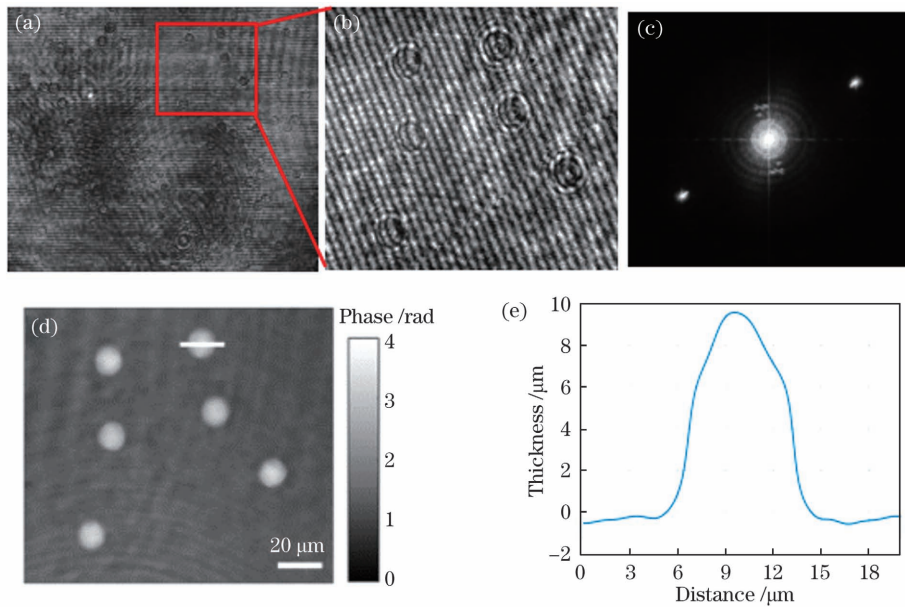

图 6　聚苯乙烯微珠的实验结果。(a) 全息图；(b) 图 6(a)中红框区域的放大图；(c) 频谱图；(d) 相位图；(e) 图 6(d)中白线部分测量的微珠厚度

Fig. 6　Experimental results of polystyrene microsphere. (a) Hologram; (b) magnified image of red border area in Fig. 6(a); (c) spectrum; (d) phase diagram; (e) microsphere thickness curve measured along white line of Fig. 6(d)

得到的微珠厚度约为 9.75 μm。为确保实验数据可靠，实验测量分析了 100 个微珠的厚度，这些数值均在 (9.8±0.2) μm 范围内，这验证了系统定量相位测量的准确性。

实验选用 1951 年美国空军分辨率测试板 (USAF1951) 作为测量成像系统分辨能力的测试对象，图 7 是该系统下的测试图像，实验采用传统的角谱方法对样品全息图进行重建，获得了强度图。为了减弱参考光光强分布不均对重建强度图的干扰，本实验采用重建获得的强度图与单一的参考光强度图相除的方法进行了简单的优化处理，获得的强度图如图 7(d)

所示。可以看出，该系统能清晰成像到第 7 组第 6 个元素，即分辨率可达到 2.19 μm，适合生物样品的成像，充分证明了该系统优秀的成像分辨率。

在生物样品成像性能检测方面，本研究选用较厚的洋葱表皮细胞作为实验对象，获得的全息图如图 8(a) 所示，图 8(b) 为所选区域的局部放大图，图 8(c)~(e) 是对应的频谱图、强度图和三维图。从局部放大图像可以看出，即使参考光光强分布受物体特性的影响，但是在全视场内，记录的干涉条纹仍能保持清晰，重建出的强度图和相位图能保证样品信息的完整。洋葱表皮细胞的折射率为1.381，图8(e)中的
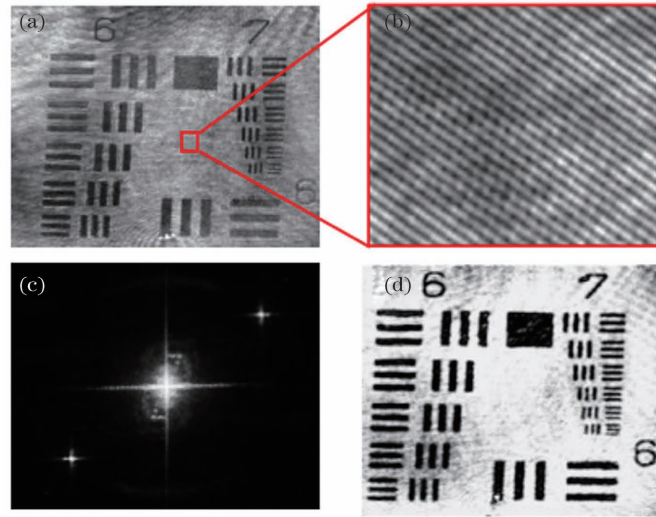
图 7　USAF1951 分辨率板的实验结果图。(a)全息图;(b)图 7(a)中红边框区域的放大图;(c)频谱图;(d)强度图

Fig. 7　Experimental results of USAF1951 resolution board. (a) Hologram; (b) magnified image of red border area in Fig. 7(a); (c) spectrum; (d) amplitude image
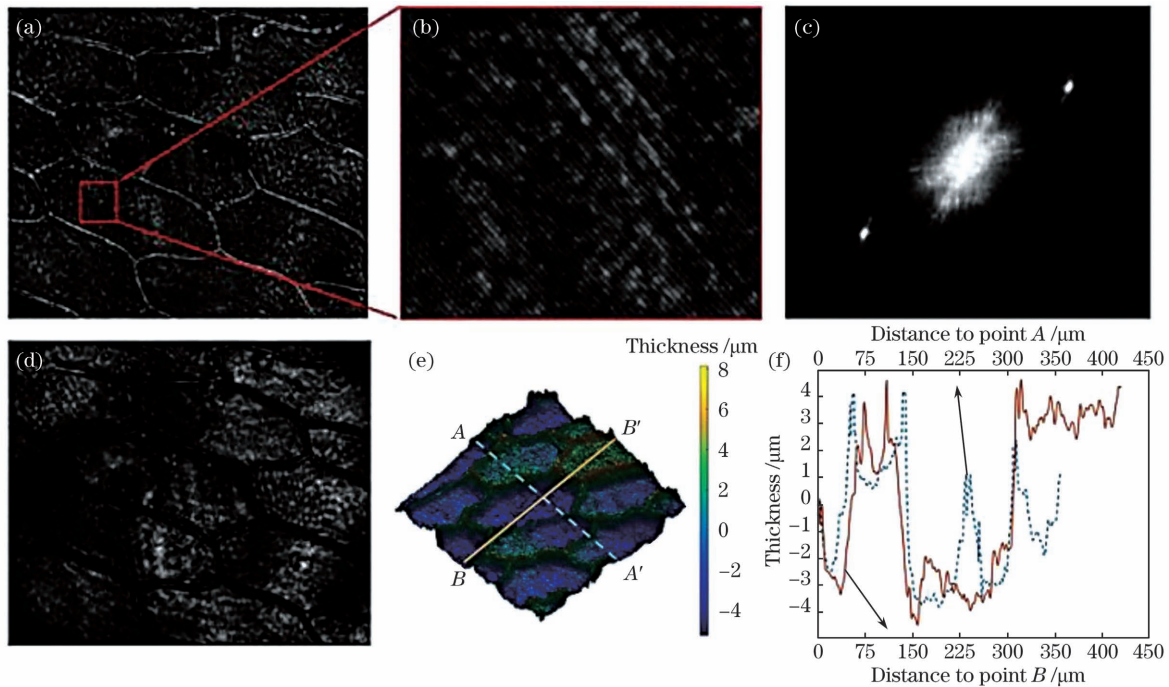
图 8　洋葱表皮细胞的实验结果图。(a)全息图;(b)图 8(a)中红框区域的放大图;(c)频谱图;(d)强度图;(e)三维图;
(f)图 8(e)中实线和虚线部分测量的洋葱厚度

Fig. 8　Experimental results of onion epidermal cells. (a) Hologram; (b) magnified image of red border area in Fig. 8(a); (c) spectrum; (d) amplitude image; (e) three-dimensional diagram; (f) onion thickness curves measured along solid line and dotted line in Fig.8(e)

细胞厚度具体数值是根据式(6)换算得到的。图 8(f)是对应的细胞实际厚度曲线。从重建的三维相位图和横向曲线图中可以获得,洋葱细胞厚度约为 $4.2\ \mu m$,单个细胞的直径约为 $190.0\ \mu m$。上述实验证明了该系统优秀的定量相位测量能力和成像分辨能力。

4　结　　论

提出了一种基于分光棱镜的共路离轴数字全息显微系统。实验结果表明:通过旋转偏振片,可实现全息图干涉条纹对比度的灵活调整和全视场干涉条纹清晰度的提高,系统灵活性得到有效提高。此外,通过旋转分束棱镜来控制物光与参考光的分离程度,可增大重建频谱图中 0 级与 ±1 级频谱的分离间距,避免出现频谱混叠现象,并扩大频谱图可滤波区域,提高记录器件的空间带宽积利用率,提升全息成像质量。所提方法为数字全息显微镜的制作提供了技术支持。

参 考 文 献

[1] 冯方, 田爱玲, 刘丙才, 等. 基于数字全息扫描成像的划痕缺陷全场三维测试[J]. 中国激光, 2020, 47(4): 0409003.
Feng F, Tian A L, Liu B C, et al. Full-field three-dimensional

test for scratch defects using digital holographic scanning imaging system[J]. Chinese Journal of Lasers, 2020, 47(4): 0409003.

[2] Di J L, Wu J, Wang K Q, et al. Quantitative phase imaging using deep learning-based holographic microscope[J]. Frontiers in Physics, 2021, 9: 651313.

[3] 董昭, 王文健, 王华英, 等. 改进的基于相位梯度最小化的相位补偿方法[J]. 中国激光, 2021, 48(24): 2409001.
Dong Z, Wang W J, Wang H Y, et al. Improved phase compensation method based on phase vibration minimization[J]. Chinese Journal of Lasers, 2021, 48(24): 2409001.

[4] Wen Y F, Wang H Y, Anand A, et al. A fast autofocus method based on virtual differential optical path in digital holography: theory and applications[J]. Optics and Lasers in Engineering, 2019, 121: 133-142.

[5] Zhong Z, Zhao H J, Cao L C, et al. Automatic cross filtering for off-axis digital holographic microscopy[J]. Results in Physics, 2020, 16: 102910.

[6] Seo K W, Choi Y S, Seo E S, et al. Aberration compensation for objective phase curvature in phase holographic microscopy[J]. Optics Letters, 37(23): 4976-4978.

[7] Lai X M, Xiao S, Xu C, et al. Aberration-free digital holographic phase imaging using the derivative-based principal component analysis[J]. Journal of Biomedical Optics, 2021, 26: 046501.

[8] 曾雅楠, 卢钧胜, 刘源, 等. 基于数字全息显微的微粒三维位移跟踪测量技术[J]. 中国激光, 2017, 44(12): 1204001.
Zeng Y N, Lu J S, Liu Y, et al. Three-dimensional displacement tracking technique of particle based on digital holographic microscopy[J]. Chinese Journal of Lasers, 2017, 44(12): 1204001.

[9] Krizova A, Collakova J, Dostal Z, et al. Dynamic phase differences based on quantitative phase imaging for the objective evaluation of cell behavior[J]. Journal of Biomedical Optics, 2015, 20(11): 111214.

[10] Gurram H P R, Panta P, Pandiyan V P, et al. Digital holographic microscopy for quantitative and label-free oral cytology evaluation[J]. Optical Engineering, 2020, 59: 024105.

[11] Lee K, Kim K, Jung J, et al. Quantitative phase imaging techniques for the study of cell pathophysiology: from principles to applications[J]. Sensors, 2013, 13(4): 4170-4191.

[12] Wu C H, Lai X J, Cheng C J, et al. Applications of digital holographic microscopy in therapeutic evaluation of Chinese herbal medicines[J]. Applied Optics, 2014, 53(27): G192-G197.

[13] Majeed H, Sridharan S, Mir M, et al. Quantitative phase imaging for medical diagnosis[J]. Journal of Biophotonics, 2017, 10(2): 177-205.

[14] Rajput S K, Matoba O, Kumar M, et al. Sound wave detection by common-path digital holography[J]. Optics and Lasers in Engineering, 2021, 137: 106331.

[15] Brito I V, Gesualdi M R, Muramatsu M, et al. Holographic microscopy techniques applied to micro-structures analysis[C]//Latin America Optics and Photonics Conference, September 27-30, 2010, Recife, Brazil. Washington, D.C.: OSA, 2010: MB34.

[16] Xia P, Ri S E, Wang Q H, et al. Nanometer-order thermal deformation measurement by a calibrated phase-shifting digital holography system[J]. Optics Express, 2018, 26(10): 12594-12604.

[17] Lee H S, Shin S, Lee H, et al. Determining two-sided surface profiles of micro-optical elements using a dual-wavelength digital holographic microscope with liquids[J]. Journal of the Optical Society of Korea, 2014, 18(5): 495-499.

[18] Eldridge W J, Sheinfeld A, Rinehart M T, et al. Imaging deformation of adherent cells due to shear stress using quantitative phase imaging[J]. Optics Letters, 2016, 41(2): 352-355.

[19] Popescu G, Ikeda T, Dasari R R, et al. Diffraction phase microscopy for quantifying cell structure and dynamics[J].

[20] Bhaduri B, Edwards C, Pham H, et al. Diffraction phase microscopy: principles and applications in materials and life sciences[J]. Advances in Optics and Photonics, 2014, 6(1): 57-119.

[21] Quan X Y, Kumar M, Rajput S K, et al. Multimodal microscopy: fast acquisition of quantitative phase and fluorescence imaging in 3D space[J]. IEEE Journal of Selected Topics in Quantum Electronics, 2021, 27(4): 1-11.

[22] Liu B C, Wang D S, Zhu X L, et al. Wavelength-tuning common-path digital holographic microscopy for quantitative phase imaging of functional micro-optics components[J]. Applied Sciences, 2020, 10(16): 5602.

[23] Baek Y, Lee K, Yoon J, et al. White-light quantitative phase imaging unit[J]. Optics Express, 2016, 24(9): 9308-9315.

[24] Kumar M, Quan X Y, Awatsuji Y, et al. Single-shot common-path off-axis dual-wavelength digital holographic microscopy[J]. Applied Optics, 2020, 59(24): 7144-7152.

[25] Shaked N T. Quantitative phase microscopy of biological samples using a portable interferometer[J]. Optics Letters, 2012, 37(11): 2016-2018.

[26] Girshovitz P, Shaked N T. Compact and portable low-coherence interferometer with off-axis geometry for quantitative phase microscopy and nanoscopy[J]. Optics Express, 2013, 21(5): 5701-5714.

[27] Bai H Y, Shan M G, Zhong Z, et al. Common path interferometer based on the modified Michelson configuration using a reflective grating[J]. Optics and Lasers in Engineering, 2015, 75: 1-4.

[28] Mahajan S, Trivedi V, Vora P, et al. Highly stable digital holographic microscope using Sagnac interferometer[J]. Optics Letters, 2015, 40(16): 3743-3746.

[29] Roitshtain D, Turko N A, Javidi B, et al. Flipping interferometry and its application for quantitative phase microscopy in a micro-channel[J]. Optics Letters, 2016, 41(10): 2354-2357.

[30] Li Y, Zhang S M, Zhang J Y, et al. Single-shot phase-shifting radial-shearing digital holography with Fibonacci-sieve array irrespective of initial phases[J]. Applied Physics Letters, 2021, 118(26): 261101.

[31] Mico V, Ferreira C, Zalevsky Z, et al. Spatially-multiplexed interferometric microscopy (SMIM): converting a standard microscope into a holographic one[J]. Optics Express, 2014, 22(12): 14929-14943.

[32] Zhang M L, Ma Y, Wang Y, et al. Polarization grating based on diffraction phase microscopy for quantitative phase imaging of paramecia[J]. Optics Express, 2020, 28(20): 29775-29787.

[33] 张佳恒, 马利红, 李勇, 等. 卤素灯照明光栅衍射共路数字全息显微定量相位成像[J]. 中国激光, 2018, 45(6): 0609003.
Zhang J H, Ma L H, Li Y, et al. Halogen-light quantitative phase imaging with common-path digital holographic microscopy based on grating diffraction[J]. Chinese Journal of Lasers, 2018, 45(6): 0609003.

[34] 郁道银, 谈恒英. 工程光学[M]. 3 版. 北京: 机械工业出版社, 2011.
Yu D Y, Tan H Y. Engineering optics[M]. 3rd ed. Beijing: China Machine Press, 2011.

[35] 钱晓凡, 王占亮, 胡特, 等. 用单幅数字全息和剪切干涉原理重构光场相位[J]. 中国激光, 2010, 37(7): 1821-1826.
Qian X F, Wang Z L, Hu T, et al. Reconstructing the phase of wavefront using digital hologram and the principle of shearing interferometry[J]. Chinese Journal of Lasers, 2010, 37(7): 1821-1826.

[36] 王华英, 刘佐强, 廖薇, 等. 基于最小范数的四种相位解包裹算法比较[J]. 中国激光, 2014, 41(2): 0209016.
Wang H Y, Liu Z Q, Liao W, et al. Comparison of four phases unwrapping algorithm based on method of minimum norm[J]. Chinese Journal of Lasers, 2014, 41(2): 0209016.

Optics Letters, 2006, 31(6): 775-777.

Common-Path Off-Axis Digital Holographic Microscopy Based on Beam Splitter

Wang Huaying[1,2 *], Lei Jialiang[1], Wang Xue[1,2], Wang Wenjian[1], Zhang Zijian[1], Wang Jieyu[1], Dong Zhao[1,2]

[1] *School of Mathematics & Physics Science and Engineering, Hebei University of Engineering, Handan* 056038, *Hebei, China*;
[2] *Hebei Computational Optical Imaging and Photoelectric Detection Technology Innovation Center, Handan* 056038, *Hebei, China*

Abstract

Objective　　The digital holographic microscopy technology can perform real-time quantitative imaging and visual measurement of phase objects and various microstructures under non-contact, non-staining experimental conditions. It plays an important role in life, medicine, environment, materials, manufacturing, and other fields. As the object and the reference beams pass through the same optical elements, the same phase noises are introduced into them. The structure makes the common path off-axis digital holographic microscopy (CO-DHM) more stable. However, the contrast of the hologram fringes recorded by the traditional CO-DHM system is often poor, and the utilization of the space bandwidth product of the recording device is insufficient. These defects seriously influence the filtering process and the quality of the reconstructed images. In this paper, a novel CO-DHM based on a beam splitter is proposed. The intensity ratio of the object and reference beams can be adjusted. The separation distance of three spectral terms in the hologram can also be flexibly controlled by this structure. The feasibility of adjusting stripe-contrast and spatial-frequency is analyzed theoretically and experimentally, and the imaging performance of the system is verified by the experimental analysis.

Methods　　The setup of the proposed CO-DHM can be referred to Fig. 1. In order to analyze the system ability to separate and regulate the object and reference beams, the lateral offset distance range of the incident beam splitter is calculated (Fig. 2). In addition, the ability to adjust the fringe contrast is introduced. The polarization states of the object and reference beams when interference occurs are analyzed by the Jones matrix. The intensity of each light and the change in the contrast of the interference fringe are analyzed in different principal-axis azimuths of the polarizer (Fig. 3).

Results and Discussions　　In the control performance of the system, we use (9.8 ± 0.2) μm highly dispersed polystyrene microsphere (refractive index $n = 1.593$) as the sample. The separation distance between the object and reference beams is modulated by laterally moving the beam splitter (Fig. 4). When the separation distance between the object and reference beams is 5 mm, the spectrum is aliased. If the spectral filter area including the zero-order center is too large, the fringe information is introduced in the phase diagram. Even if the filtering area is reduced, the low-frequency information of the 0 order is still introduced, which brings noise interference to the reconstructed phase diagram. When the separation distance between the object and reference beams is 9 mm, the spatial-frequency is separated fully, which avoids the above situation. It is helpful for the reconstruction of digital holography. In order to analyze the influence of interference fringe contrast on the experiment, we modulate the light intensity ratio of the object and reference beams to 1:1, 6:1, and 34:1 by rotating the polarizer (Fig. 5). It can be seen that the fringe contrast of the hologram is significantly reduced as the light intensity ratio increases and the ± 1 orders bandwidths are also reduced. The noise carried by the object beam is more obvious, and the quality of the reconstructed image becomes worse. Therefore, adjusting the contrast of interference fringes is an important part of digital holographic recording. In this system, the light intensity ratio of the object reference beams can be adjusted flexibly, which can effectively avoid the occurrence of the above situation. In the imaging performance of the system, the same polystyrene microsphere sample is used to perform a quantitative imaging test (Fig. 6). It can be seen that the reconstructed microsphere thickness is about 9.75 μm. In order to ensure the reliability of the experiment, the thickness of 100 microspheres is measured and analyzed, and the values are all within the range of (9.8 ± 0.2) μm, which satisfies the nominal diameters of the microspheres and verifies that the quantitative phase measurement is accurate. We test the capability of the resolution by imaging the standard USAF1951 resolution plate (Fig. 7). It can be seen that the system can clearly image the sixth element of the 7 groups, which means that the resolution can reach 2.19 μm. It is suitable for the imaging of biological samples, which fully proves that the system has excellent imaging resolution. Onion epidermal cells are used as the experimental object (Fig. 8). The experimental results show that the thickness of onion cells is about 4.2 μm and the size of individual cells is about 190.0 μm, which fully proves that the system has excellent imaging performance for biological samples.

Conclusions   The experimental results show that the effect of arbitrarily adjusting the contrast of the hologram interference fringe is achieved by rotating the polarizer, the flexibility of the system is effectively improved. In addition, the degree of separation between the object and reference beams is controlled by rotating the beam splitter. The separation distance between the 0 order and ±1 orders in the Fourier transform is increased to extend a filterable region and avoid spectral aliasing. The method in this paper provides a technical support for the production of digital holographic microscopes.

Key words   holography；digital holography；microscopy；quantitative phase measurement；spectral filtering